




Article

Characterization of Synthetic Non-Metallic Inclusions Consisting of TiN, Ti₂O₃, and Oxides of Al₂O₃ and MgO·Al₂O₃ Spinel Using Raman Spectroscopy

Francis Gyakwaa ^{1,*} , Tuomas Alatarvas ¹ , Qifeng Shu ¹ , Matti Aula ^{1,2} and Timo Fabritius ¹ 

¹ Process Metallurgy Research Unit, University of Oulu, P.O. Box 4300, FI-90014 Oulu, Finland; Tuomas.Alatarvas@oulu.fi (T.A.); Qifeng.Shu@oulu.fi (Q.S.); Matti.Aula@oulu.fi (M.A.); timo.fabritius@oulu.fi (T.F.)

² Luxmet Ltd., Paavo Havaksen tie 5 D, FI-90570 Oulu, Finland

* Correspondence: Francis.gyakwaa@oulu.fi

Abstract: Steel quality and properties can be affected by the formation of complex inclusions, including Ti-based inclusions such as TiN and Ti₂O₃ and oxides like Al₂O₃ and MgO·Al₂O₃ (MA). This study assessed the prospective use of Raman spectroscopy to characterize synthetic binary inclusion samples of TiN–Al₂O₃, TiN–MA, Ti₂O₃–MA, and Ti₂O₃–Al₂O₃ with varying phase fractions. The relative intensities of the Raman peaks were used for qualitative evaluation and linear regression calibration models were used for the quantitative prediction of individual phases. The model performance was evaluated with root mean square error of cross-validation (RMSECV) and root mean square error of prediction (RMSEP). For the raw Raman spectra data, R² values were between 0.48–0.98, the RMSECV values varied between 3.26–14.60 wt%, and the RMSEP ranged between 2.98–15.01 wt% for estimating the phases. The SNV Raman spectra data had estimated R² values within 0.94–0.99 and RMSECV and RMSEP values ranged between 2.50–3.26 wt% and 2.80–9.01 wt%, respectively, showing improved model performance. The study shows that the specific phases of TiN, Al₂O₃, MA, and Ti₂O₃ in synthetic inclusion mixtures of TiN–(Al₂O₃ or MA) and Ti₂O₃–(Al₂O₃ or MA) could be characterized by the Raman spectroscopy.

Keywords: Raman spectroscopy; Ti-based inclusions; MgO·Al₂O₃ spinel; aluminum oxide; characterization



Citation: Gyakwaa, F.; Alatarvas, T.; Shu, Q.; Aula, M.; Fabritius, T. Characterization of Synthetic Non-Metallic Inclusions Consisting of TiN, Ti₂O₃, and Oxides of Al₂O₃ and MgO·Al₂O₃ Spinel Using Raman Spectroscopy. *Metals* **2021**, *11*, 1549. <https://doi.org/10.3390/met11101549>

Academic Editor: Alexander Ivanovich Zaitsev

Received: 15 August 2021

Accepted: 24 September 2021

Published: 28 September 2021

Publisher's Note: MDPI stays neutral with regard to jurisdictional claims in published maps and institutional affiliations.



Copyright: © 2021 by the authors. Licensee MDPI, Basel, Switzerland. This article is an open access article distributed under the terms and conditions of the Creative Commons Attribution (CC BY) license (<https://creativecommons.org/licenses/by/4.0/>).

1. Introduction

The addition of titanium to steel plays several essential roles, such as acting as a deoxidizing agent or binding nitrogen to prevent BN formation in boron-alloyed steels [1]. In addition, titanium may also affect the mechanical properties of the final product [2,3]. However, earlier investigations have demonstrated the formation of Ti-based inclusions, such as TiN and Ti₂O₃, in steels and their potentially detrimental effect on the steel properties [4,5]. Furthermore, numerous studies [6–8] have shown that the presence of TiN or Ti₂O₃ inclusions generated during steelmaking or in final steel products could occur as a mixture with other detrimental oxide inclusion phases. For instance, studies [6–8] further suggested that the addition of Ti and the potential generation of TiN precipitates could lead to the possible formation of a complex inclusion of Al₂O₃–TiN [6,8] or TiN–MgO·Al₂O₃ spinel [7] during steel solidification and, thus, in the final steel products. Furthermore, inclusion phase mixtures, such as Ti₂O₃ with Al₂O₃ or MgO·Al₂O₃, could be generated during steel solidification depending on the composition of the steel melt. These binary or complex inclusion mixtures complicate the ability to achieve clean steel; therefore, it is essential to characterize them.

The application of various analytical techniques, such as scanning electronic microscope with energy dispersive spectroscopy (SEM-EDS) and others classified by Zhang et al. [9], has

contributed immensely to characterizing inclusions commonly found in steel. However, the general expectations concerning the analytical technique used for identification and analysis of inclusions are to that it has features such as a relatively short duration of sample preparation, improved accuracy, and reliable analysis results, as these are of interest to researchers and steelmakers. Raman spectroscopy has been demonstrated to be a robust method and has most of these features. Consequently, Raman spectroscopy is a prospective analytical tool for inclusion characterization compared to other methods, such as SEM-EDS, in terms of sample preparation and analysis duration.

Previous studies have demonstrated the prospective application of Raman characterizing oxide mixtures from Al_2O_3 , $\text{MgO}\cdot\text{Al}_2\text{O}_3$ spinel (MA), and calcium aluminates from synthetic inclusions phase [10]. In addition, the study conducted by S. Li and Hihara (2017) [11] has shown that individual phases of calcium-aluminate-based inclusions, such as $\text{CaO}\cdot\text{Al}_2\text{O}_3$ (CA), in steel samples could be identified in steel samples using Raman spectroscopy. Furthermore, Matsuura et al. [12] and Pan et al. [13] have shown the possibility for Ti-based inclusion occurring as a mixture with oxides in steel samples, while TiN and Ti_2O_3 interactions with slag towards steel cleanliness was demonstrated by Michelic et al. [14]. However, fewer studies have been conducted concerning the use of Raman spectroscopy for detailed characterization for a mixture of phases, such as TiN and Ti_2O_3 with other oxide inclusions, like $\text{MgO}\cdot\text{Al}_2\text{O}_3$ spinel and Al_2O_3 , and the use of a calibration model to quantify the relative content of the phases present. For instance, studies conducted by [15,16] demonstrated the use of Raman spectroscopy to mainly identify Ti-based inclusions phases such as TiN, Ti_2O_3 , and other phases from Ti-deoxidation process-based products [15] and under different experimental conditions [16], but not for predicting the individual phase content using calibration model as shown in this work. Consequently, there is a need to expand the scope concerning the potential use of Raman spectroscopy for inclusion studies since inclusions generated in steels could occur as a mixture of phases, as illustrated by previous research. Consequently, the purpose of this work was to demonstrate the prospect of the application of Raman spectroscopy as an analytical technique to identify and characterize synthetic inclusion mixtures consisting of titanium nitride (TiN), aluminum oxide (Al_2O_3), magnesium–aluminate spinel ($\text{MgO}\cdot\text{Al}_2\text{O}_3$, MA), and Ti_2O_3 . Here, binary phases of TiN– Al_2O_3 , TiN–MA, Ti_2O_3 –MA, and Ti_2O_3 – Al_2O_3 were investigated.

2. Materials and Methods

The synthetic binary phase samples prepared for this study were TiN– Al_2O_3 , TiN–MA, Ti_2O_3 –MA, and Ti_2O_3 – Al_2O_3 . The chemical powders used for this work were titanium nitride (TiN), magnesium aluminate spinel $\text{MgO}\cdot\text{Al}_2\text{O}_3$ (MA), titanium (III) oxide (Ti_2O_3), and aluminum oxide (Al_2O_3). These chemicals were obtained from commercial suppliers; Sigma-Aldrich (Merck KGaA, Darmstadt, Germany) and Alfa Aesar (Erlenbachweg 2 76870, Kandel Germany), with purity in the range of 99.7% to 99.9%. The required proportions (weight percentage) of the phases (TiN, $\text{MgO}\cdot\text{Al}_2\text{O}_3$, Al_2O_3 , and Ti_2O_3) were measured by using an analytical balance. The weighed samples were milled to achieve a uniform size and sample homogeneity. The milling further ensured that the samples inside each spectrum acquired during the Raman spectroscopy measurements would represent the phases present in the binary sample prepared. For synthetic samples containing TiN–(Al_2O_3 or MA), the phase fraction of TiN was varied between 10 wt% and 90 wt% for each binary phase sample (TiN– Al_2O_3 , TiN–MA). Similarly, the phase fraction of TiN for a sample matrix consisting of Ti_2O_3 –(MA or Al_2O_3) was varied approximately from 10 wt% to 90 wt% to generate binary phase mixtures of Ti_2O_3 –MA and Ti_2O_3 – Al_2O_3 .

Thorough and careful mixing was performed several times to ensure that the prepared synthetic binary phase samples were homogenous. The confirmation of the prepared samples' homogeneity was carried by using X-ray fluorescence (XRF) and X-ray diffraction (XRD) analysis techniques based on measuring replicates of the same synthetic binary phase sample. Additionally, XRF and XRD were used as complementary analytical techniques to evaluate and verify the phases present in the samples. The chemical and phase composition

of the starting chemicals (TiN, Al₂O₃, Ti₂O₃, and MgO·Al₂O₃) were evaluated by using XRD and XRF. Details concerning setup parameters for XRD and XRF instruments used for this study were explained in our previous work [10]. Tables 1 and 2 illustrates a comparison between the weight percentages of the phases (TiN, Al₂O₃, MA, and Ti₂O₃) measured by using analytical balance for generating the sample mixtures and specific phases calculated based on the XRF elemental analysis.

Table 1. Prepared sample composition and XRF analyses obtained from binary phases of Ti₂O₃–Al₂O₃ and Ti₂O₃–MA.

Initial Phase Composition (wt%)		Phases Calculated Based on XRF Analysis (wt%)		Initial Phase Composition (wt%)		Phases Calculated Based on XRF Analysis (wt%)	
Ti ₂ O ₃	Al ₂ O ₃	Ti ₂ O ₃	Al ₂ O ₃	MgO·Al ₂ O ₃	Ti ₂ O ₃	MgO·Al ₂ O ₃	Ti ₂ O ₃
90	10	90.3	9.7	10	90	9.0	91.0
80	20	81.6	18.4	20	80	18.0	82.0
70	30	74.5	25.5	30	70	32.1	67.9
60	40	58.0	42.0	40	60	39.0	61.0
55	45	52.0	48.0	45	55	47.5	52.5
50	50	48.5	51.5	50	50	51.0	49.0
40	60	35.9	64.1	60	40	73.7	26.3
30	70	28.0	72.0	70	30	65.5	34.5
20	80	21.0	79.0	80	20	82.3	17.7
10	90	7.0	93.0	90	10	91.0	9.0

Table 2. Prepared sample composition and XRF analyses obtained from binary phases of TiN–Al₂O₃ and TiN–MA.

Initial Phase Composition (wt%)		Phases Calculated Based on XRF Analysis (wt%)		Initial Phase Composition (wt%)		Phases Calculated Based on XRF Analysis (wt%)	
TiN	Al ₂ O ₃	TiN	Al ₂ O ₃	MgO·Al ₂ O ₃	TiN	MgO·Al ₂ O ₃	TiN
10	90	9.0	91.0	10	90	8.0	92.0
20	80	16.0	84.0	20	80	22.0	78.0
30	70	28.8	71.2	30	70	28.8	71.2
40	60	36.8	63.2	40	60	36.8	63.2
50	50	46.7	53.3	45	55	46.7	53.3
60	40	53.0	47.0	50	50	52.0	48.0
70	30	56.7	43.3	60	40	56.7	43.3
80	20	75.3	24.7	70	30	75.3	24.7
90	10	83.9	16.1	80	20	83.9	16.1
				90	10	91.2	8.8

2.1. Raman Spectroscopy

The Raman spectroscopy used for this study was TimeGated[®] Raman spectrometer (TG532 M1) from Timegate instruments limited, Oulu, Finland. Details concerning the features for the Raman spectroscopy used to conduct the measurements have been presented in previous studies by the authors of this study [10]. The same parameter settings associated with the Raman spectroscopy, such as a resolution of 10 cm^{−1} laser power (545) and duration for spectra acquisition, were used during the prepared sample measurements. The Raman spectra obtained from the Raman spectroscopy measurements were within the Raman shift region between 100–1100 cm^{−1} and under ambient conditions. During the Raman measurements, some procedures were used to achieve relatively enhanced repeatability and decrease the challenges associated with sample inhomogeneity. These included total spectra with at least three replicates collected at different spots for each sample, and the spectra acquisition duration was between 1–3 min.

Additionally, the Raman spectroscopy setup was equipped with a rotating sample holder stage, making it possible to obtain an average Raman spectrum at the different spots of each batch of the sample measured. The pre-processing software (from Timegate instrument Limited) was used for the initial Raman spectra data treatment, such as basic background subtraction. Other statistical software programs, such as OriginPro, 2020 and an unscrambler (version 11.0, by Camo Software, Oslo, Norway), were used for subsequent Raman spectra pre-processing, peak fitting, and multivariate analysis. A Gaussian peak shape was used for the Raman peak fitting since it was generally demonstrated to be suitable for the solid samples prepared and measured with the Raman spectroscopy. Further explanation concerning the selection of this peak shape can be found in [17].

2.2. Calibration Model

A calibration model and multivariate analysis were used to establish a relationship between the specific phase content present in the samples and the identified Raman peak ratios. The variation in the phase content (wt%) present in the sample was evaluated by using the summed Raman spectrum to explain the relative integrated areas of the identified peaks present in the Raman spectrum. The calibration candidate is expressed as:

$$x_c = \frac{A_m}{(A_n + A_m)}, \quad (1)$$

where x_c is the calibration feature candidate, A_m is the integrated area for the Raman peak n , and A_n is the area corresponding to the Raman peak n .

Evaluation of the model performance for each calibration feature candidate was carried out using partial least squares (PLS) regression for this study [18]. The PLS regression method was first carried out with the raw Raman spectral data from the Raman measurement and, subsequently, on pre-processed Raman spectra data by using the standard normal variate (SNV) technique. Studies have shown that the application of SNV to raw spectral data provides some benefits for subsequent analysis of the data [19]. These include minimizing the potential baseline shifting and reducing some possible sources of non-linearity linked with the phase content of the analyses associated with the measured Raman spectra [19]. This can help evaluate the performance of a PLS regression method when the raw Raman spectra data are used, comparing these to the pre-processed Raman spectra data measured from the multiphase samples.

In performing the PLS analysis, the obtained Raman spectra data were randomly split into calibration (training) and the prediction (external validation) sets. Approximately 75% of the samples were used as the calibration set to obtain the quantification model. The remaining randomly split samples of 25% were used as the prediction set for testing the model. In this study, Raman spectra from 100 to 900 cm^{-1} were identified as being suitable to use for the PLS model since most of the dominant Raman peaks for the phases used in preparing the samples were within this region. The accuracy of the model was carried out using the cross-validation process with the leave-one-out cross-validation technique. More details concerning the PLS analysis procedure for this study can be found in [20,21].

In evaluating the performance of the calibration model used for estimating the phase content in the prepared samples, three performance indicators were used for the calibration set [21,22]. These were the coefficient of determination (R^2), the root mean standard error in calibration (RMSEC), and the root mean standard error in cross-validation (RMSECV). Similarly, the coefficient of determination and root mean square error of prediction (RMSEP) were used to assess the external validation (prediction) or test set performance. According to Kachrimanis et al. [22], the root mean standard error (RMSE) can be given as:

$$\text{RMSE} = \sqrt{\frac{\sum_{i=1}^n (y_i - \hat{y}_i)^2}{n}} \quad (2)$$

where y_i represents the reference value, and the number of samples marked as n and \hat{y} denote the calculated value.

3. Results

3.1. Raman Spectra Analysis Based on Phase Content

The identifiable Raman bands (peaks) assigned to each phase (TiN, MgO·Al₂O₃, Al₂O₃, and Ti₂O₃) were used to prepare the synthetic inclusion samples and some referenced studies are presented in Table 3. Figure 1 shows the Raman spectra for synthetic inclusion phases of TiN, MgO·Al₂O₃, Al₂O₃, and Ti₂O₃ used to prepare the binary samples consisting of TiN–Al₂O₃, TiN–MA, Ti₂O₃–MA, and Ti₂O₃–Al₂O₃. The Raman spectra for starting phases are arranged from the top in Figure 1 as follows: spectrum for TiN (Figure 1i), spectrum for MgO·Al₂O₃ (Figure 1ii), spectrum for Al₂O₃ (Figure 1iii), and spectrum for Ti₂O₃ (Figure 1iv).

Table 3. Measurement Raman peaks (bands) for the synthetic phase used for this study (where s is strong, m is medium, and w is weak).

Phase	Measured Peaks [Raman Shift, cm ⁻¹]	Reference Peaks [Raman Shift, cm ⁻¹]	Reference
TiN	157 s, 260 m, 620 m	152 s, 340 m, 410 m, 620 m,	[23]
Al ₂ O ₃	422 s, 383 m, 760 m,	413–420 s, 375–380 m, 758 m,	[24]
MgO·Al ₂ O ₃	416 s, 674 m, 773 m	409–412 s, 666–674 m, 767–772 m	[25]
Ti ₂ O ₃	247 s, 335 m,	247 s, 336 m, 423 w	[26]

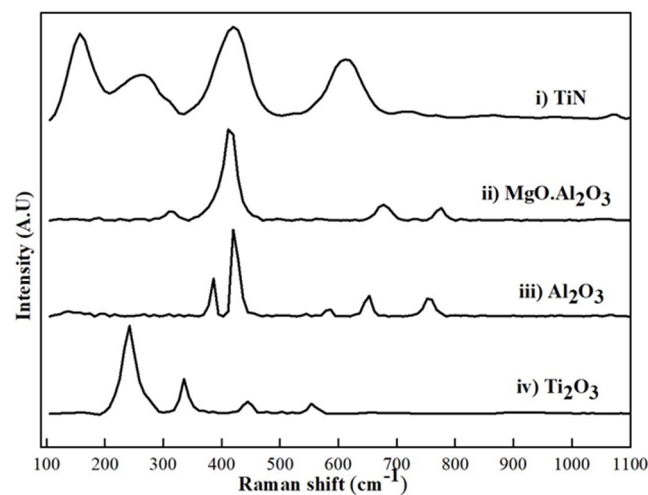


Figure 1. The starting sample phases of TiN, MgO·Al₂O₃, Al₂O₃, and Ti₂O₃ Raman spectra used to prepare binary samples for this study.

3.2. Qualitative Analysis of Phase Content Based on Raman Spectra

Figures 2 and 3 show some examples from the relationship between the change in the phase content in the samples measured using Raman spectroscopy and the observable effects on the Raman peak intensities. This phenomenon, where a variation in the phase content in the binary samples has a corresponding impact on relative Raman peak intensities, provides an opportunity to quickly conduct qualitative analysis for the phases present in the samples.

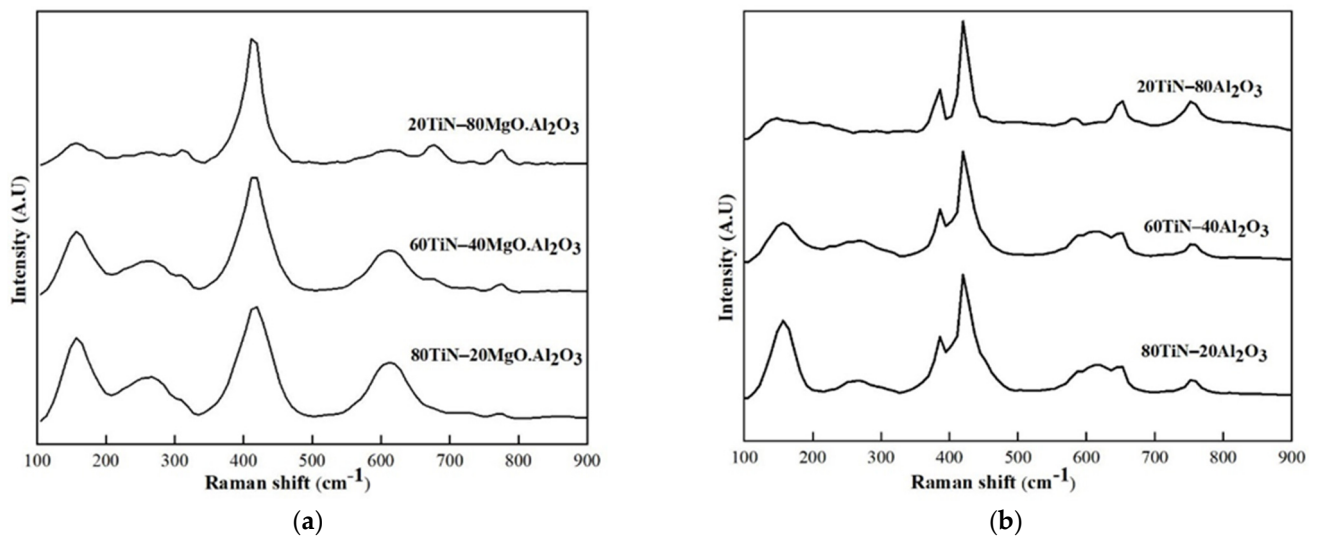


Figure 2. Raman spectra measured from binary samples used to establish a relationship between the phase content and relative peak intensity, where (a) is for TiN–MgO·Al₂O₃ and (b) is for TiN–Al₂O₃.

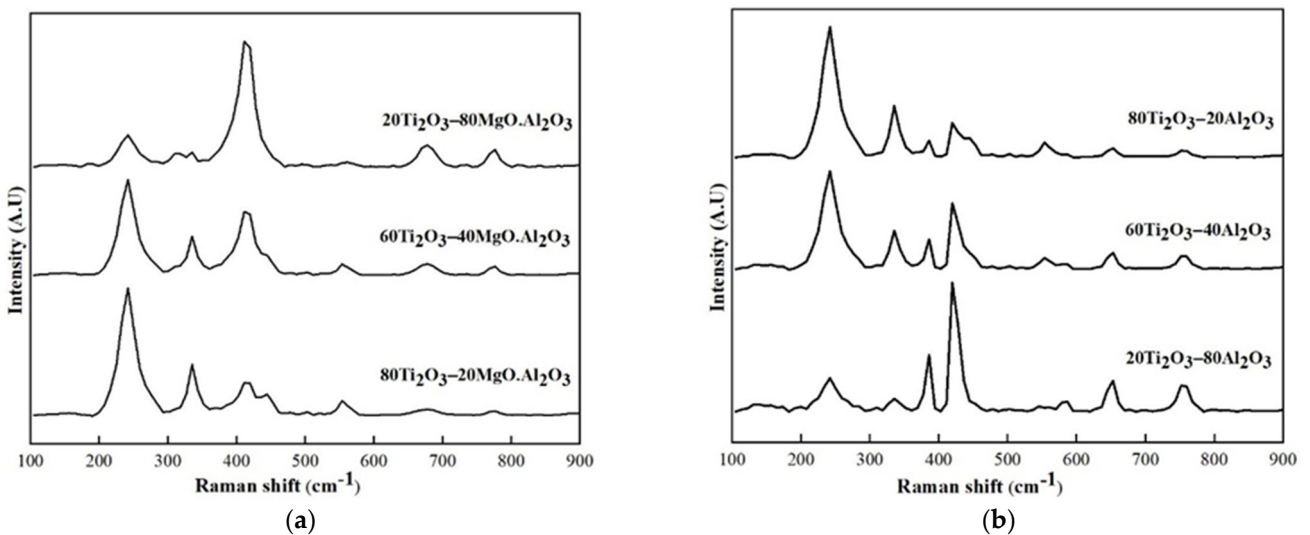


Figure 3. Raman spectra measured from binary samples used to establish a relationship between the phase content and relative peak intensity, where (a) is for Ti₂O₃–MgO·Al₂O₃ and (b) is for Ti₂O₃–Al₂O₃.

3.2.1. TiN–Al₂O₃ and TiN–MgO·Al₂O₃ (MA)

Figure 2 consists of a sample's matrix with a varying phase fraction of TiN, Al₂O₃, and MA. Figure 2a contains selected binary samples for TiN–MA with phase fractions for MA varying between 20, 40, and 80 wt% in each sample. Similarly, Figure 2b shows examples of TiN–Al₂O₃ with the phase content for Al₂O₃ varying between 20, 40, and 80 wt%. It is observable from Figure 2a that variation (increase or decrease) in MA content for samples containing TiN–MA had a responding effect on the Raman peak intensity at 773 cm^{−1}. Based on the Raman spectra observation presented in Figure 2b, a Raman peak at 157 cm^{−1} is attributable to TiN changes in relative peak intensity as the phase content (wt%) in TiN–Al₂O₃ samples varied. Additionally, for the TiN–Al₂O₃ samples, an increase in the phase fraction of Al₂O₃ exhibited an increase of a Raman peak shoulder at the region of 383 cm^{−1}. Furthermore, it was noticed that Al₂O₃ and MA phases had the most intense Raman peak (422 cm^{−1} for Al₂O₃ and 416 cm^{−1} for MA), found within a similar region as some Raman peaks associated with TiN (between 375–450 cm^{−1}), with a high potential for

peak overlap. Consequently, the medium Raman peaks could be used to relate the specific phase content in the sample as a function of its relative intensity.

3.2.2. $\text{Ti}_2\text{O}_3\text{-Al}_2\text{O}_3$, $\text{Ti}_2\text{O}_3\text{-MgO}\cdot\text{Al}_2\text{O}_3$ (MA)

Figure 3a illustrates Raman spectra for binary samples containing a mixture of Ti_2O_3 and MA, with the phase content varying between 20, 60, and 80 wt%. It was observed that a rise in the MA phase content (wt%) in the $\text{Ti}_2\text{O}_3\text{-MA}$ samples also led to an increase in the Raman peak intensity within the region of $410\text{-}420\text{ cm}^{-1}$. Figure 3b presents examples of $\text{Ti}_2\text{O}_3\text{-Al}_2\text{O}_3$ prepared with the phase fraction for Al_2O_3 varying between 20, 40, and 80 wt%. It was noticed from the Raman spectra presented in Figure 3b that with an incremental increase in the phase content of Al_2O_3 in the binary samples ($\text{Ti}_2\text{O}_3\text{-Al}_2\text{O}_3$), the Raman peak intensity associated with Al_2O_3 at 382 and 422 cm^{-1} rose relatively to correspond to the increasing content of Al_2O_3 . Similarly, in Figure 3a,b, a change in relative Raman peak intensity at approximately 247 cm^{-1} due to a variation in the phase fraction of Ti_2O_3 in $\text{Ti}_2\text{O}_3\text{-Al}_2\text{O}_3$ and $\text{Ti}_2\text{O}_3\text{-MgO}\cdot\text{Al}_2\text{O}_3$ samples was observed. Therefore, for synthetic inclusion phases containing Ti_2O_3 , Al_2O_3 , and $\text{MgO}\cdot\text{Al}_2\text{O}_3$, the relative intense Raman peaks associated with the specific phases could be used for qualitative estimation.

3.3. Quantitative Estimation of the Phase Fractions in the Samples

For quantitative estimation of the individual phases in the binary samples of $\text{TiN-Al}_2\text{O}_3$, $\text{TiN-MgO}\cdot\text{Al}_2\text{O}_3$, $\text{Ti}_2\text{O}_3\text{-Al}_2\text{O}_3$, and $\text{Ti}_2\text{O}_3\text{-MgO}\cdot\text{Al}_2\text{O}_3$, a linear calibration model was utilized. The calibration model was used to establish the relative Raman peak area and phase content in the samples. The relative Raman peak areas were estimated using Equation 1 for each of the peaks attributable to specific phases in the Raman spectra measured, and phase content based on XRF analysis was used as the dependent variable. Raman peaks at approximately 157 , 260 , and 620 cm^{-1} were used for TiN ; 247 and 335 cm^{-1} peaks were associated with Ti_2O_3 ; 382 , 422 , and 760 cm^{-1} peaks were used for Al_2O_3 ; and 416 , 674 , and 773 cm^{-1} peaks were used for $\text{MgO}\cdot\text{Al}_2\text{O}_3$ for relative Raman peak area calculations and analyses. The Raman peaks presented for calculations and analysis for TiN , Ti_2O_3 , MA, and Al_2O_3 are listed in Table 4. These Raman peak areas were used to estimate a linear regression between the phase content in the sample and the relative area Raman peak. The range of coefficient of determination (R^2) values obtained from the linear regression model by using relative integrated Raman peak area, and phase content in the samples were $0.72\text{-}0.99$ for (i) $\text{TiN-Al}_2\text{O}_3$, $0.86\text{-}0.97$ for (ii) $\text{Ti}_2\text{O}_3\text{-Al}_2\text{O}_3$, $0.93\text{-}0.98$ for (iii) $\text{Ti}_2\text{O}_3\text{-MgO}\cdot\text{Al}_2\text{O}_3$, and (iv) $0.79\text{-}0.98$ for $\text{Ti}_2\text{O}_3\text{-MgO}\cdot\text{Al}_2\text{O}_3$, which are presented in Table 4.

Table 4. Estimation of the coefficient of determination (R^2) between the relative Raman peak area and phase content from XRF analysis for (a) $\text{TiN-Al}_2\text{O}_3$, (b) $\text{Ti}_2\text{O}_3\text{-Al}_2\text{O}_3$, (c) $\text{TiN-MgO}\cdot\text{Al}_2\text{O}_3$, and (d) $\text{Ti}_2\text{O}_3\text{-MgO}\cdot\text{Al}_2\text{O}_3$.

System	Relative Intensity	R^2	System	Relative Intensity	R^2
(i) $\text{TiN-Al}_2\text{O}_3$	382/157	0.99	(iii) $\text{TiN-MgO}\cdot\text{Al}_2\text{O}_3$	674/157	0.91
	382/260	0.74		674/260	0.97
	422/157	0.94		416/157	0.98
	422/260	0.72		422/260	0.96
	760/157	0.98		773/157	0.98
	760/335	0.87		773/335	0.95
	382/620	0.88		674/620	0.93
	760/620	0.95		773/620	0.97
(ii) $\text{Ti}_2\text{O}_3\text{-Al}_2\text{O}_3$	382/247	0.86	(iv) $\text{Ti}_2\text{O}_3\text{-MgO}\cdot\text{Al}_2\text{O}_3$	416/247	0.98
	382/335	0.95		416/335	0.95
	422/247	0.97		674/247	0.81
	422/335	0.93		674/335	0.89
	760/247	0.90		774/247	0.79
	760/335	0.95		774/335	0.87

Figure 4 shows the best possible Raman peaks ratios for estimating the phase contents based on the relative integrated Raman peak area for $\text{MgO}\cdot\text{Al}_2\text{O}_3$ (MA) as a function of the phase content of MA in $\text{Ti}_2\text{O}_3\text{-MgO}\cdot\text{Al}_2\text{O}_3$ (Figure 4a) and $\text{TiN-MgO}\cdot\text{Al}_2\text{O}_3$ (Figure 4b) samples. In addition, Figure 5 illustrates the best possible Raman peaks ratios for estimating the phase contents based on the relative integrated Raman peak area for Al_2O_3 (wt%) as a function of the phase content of Al_2O_3 in $\text{Ti}_2\text{O}_3\text{-Al}_2\text{O}_3$ (Figure 5a) and $\text{TiN-Al}_2\text{O}_3$ (Figure 5b) samples. Further estimation of the individual phases in the samples prepared was performed with a PLS regression model to establish the relationship between the Raman signals and the phase concentration (wt%) in the samples prepared.

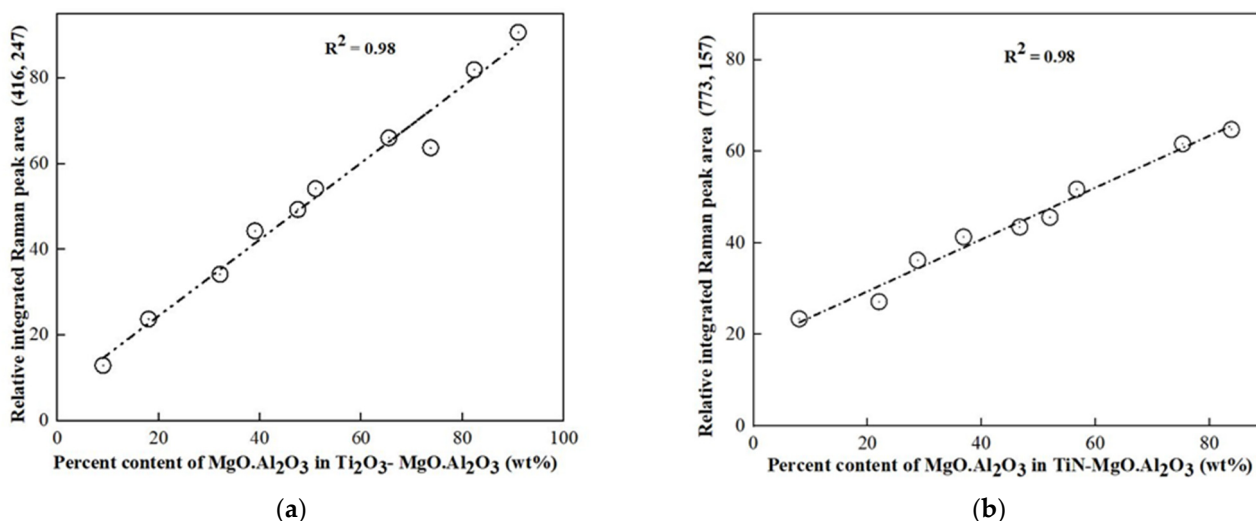


Figure 4. Estimation of phase contents based on relative integrated Raman peak area as a function of the phase content of MA in (a) $\text{Ti}_2\text{O}_3\text{-MgO}\cdot\text{Al}_2\text{O}_3$ and (b) $\text{TiN-MgO}\cdot\text{Al}_2\text{O}_3$.

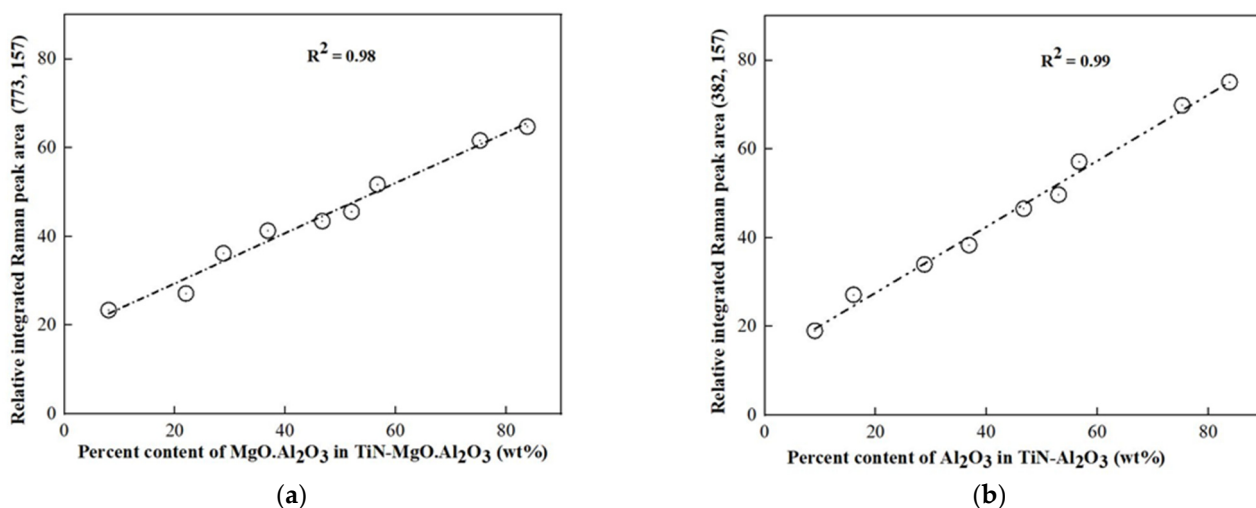


Figure 5. Estimation of phase contents based on relative integrated Raman peak area as a function of the phase content of MA in (a) $\text{Ti}_2\text{O}_3\text{-Al}_2\text{O}_3$ and (b) $\text{TiN-Al}_2\text{O}_3$.

3.4. Further Phase Estimation Assessment

The PLS regression model was first applied to the raw Raman spectral data and pre-processed Raman spectra to evaluate the phases present in the binary samples. Tables 5 and 6 present the statistical parameters and evaluated values obtained from the coefficient of determination for calibration (R^2_{CAL}), validation (R^2_{CV}), prediction (R^2_{PRED}), the root mean square of calibration (RMSEC), the root mean square of cross-validation (RMSECV),

and the root mean square error of prediction (RMSEP). Table 5 illustrates the model performance values from a PLS regression analysis to evaluate the phases (TiN, MA, and Al₂O₃) used to prepare TiN–MA and TiN–Al₂O₃ samples. The raw Raman data used to evaluate the MA phase content in TiN–MA and Ti₂O₃–MA had the following range of values for the figure of merits: R²_{CAL} (0.61–0.94), R²_{CV} (0.48–0.97), R²_{PRED} (0.61–0.95), RMSEC (5.0–14.7 wt%), RMSECV (6.0–18.1 wt%), and RMSEP (5–14.7 wt%). For pre-processed (SNV) Raman data obtained from the samples, MA phase content for R²_{CAL}, R²_{CV}, and R²_{PRED} values ranged between 0.97–0.99 and the RMSEC, RMSECV, and RMSEP ranged between 2.5–5.5 wt%. Similarly, for the raw Raman data, Al₂O₃ phase fraction analysis in TiN–Al₂O₃ and Ti₂O₃–Al₂O₃ had estimated figures of merit values varying between R²_{CAL} (0.86–0.99), R²_{CV} (0.79–0.99), R²_{PRED} (0.58–0.98), RMSEC (3.0–11.60 wt%), RMSECV (3–15.5 wt%), and RMSEP (2.9–15.11 wt%). Using SNV Raman data for the analysis, Al₂O₃ phase content estimation also had R²_{CAL}, R²_{CV}, and R²_{PRED} values varying between 0.94–0.98 and 2.98–9.20 wt% for RMSEC, RMSECV, and RMSEP values.

Table 5. Estimated figures of merit for calibration and validation using the PLS models for (i) TiN–Al₂O₃ and (ii) TiN–MgO·Al₂O₃.

System	Phase	Method	R ² _{CAL}	R ² _{CV}	R ² _{PRED}	RMSEC, (wt%)	RMSECV, (wt%)	RMSEP, (wt%)
(i) TiN–Al ₂ O ₃	TiN	Raw Data	0.86	0.79	0.58	11.56	15.14	15.01
		SNV Data	0.95	0.94	0.84	6.68	7.79	9.08
	Al ₂ O ₃	Raw Data	0.86	0.79	0.58	11.56	15.14	15.11
		SNV Data	0.96	0.95	0.94	6.11	7.71	9.07
(ii) TiN–MgO·Al ₂ O ₃	TiN	Raw Data	0.61	0.48	0.61	14.63	18.10	14.63
		SNV Data	0.99	0.99	0.98	2.60	3.10	3.01
	MgO·Al ₂ O ₃	Raw Data	0.86	0.79	0.81	11.83	13.99	14.14
		SNV Data	0.98	0.99	0.98	2.94	2.97	3.12

Table 6. Estimated figures of merit for calibration and validation using the PLS models for (i) Ti₂O₃–Al₂O₃ and (ii) Ti₂O₃–MgO·Al₂O₃.

System	Phase	Method	R ² _{CAL}	R ² _{CV}	R ² _{PRED}	RMSEC, (wt%)	RMSECV, (wt%)	RMSEP, (wt%)
(i) Ti ₂ O ₃ –Al ₂ O ₃	Ti ₂ O ₃	Raw Data	0.98	0.98	0.98	3.26	3.57	2.98
		SNV Data	0.99	0.98	0.98	3.26	3.64	2.98
	Al ₂ O ₃	Raw Data	0.99	0.99	0.98	3.11	3.68	2.94
		SNV Data	0.98	0.99	0.98	3.35	3.70	2.95
(ii) Ti ₂ O ₃ –MgO·Al ₂ O ₃	Ti ₂ O ₃	Raw Data	0.94	0.97	0.95	5.14	6.09	5.75
		SNV Data	0.98	0.98	0.97	4.81	3.22	3.02
	MgO·Al ₂ O ₃	Raw Data	0.93	0.96	0.94	5.23	6.46	7.17
		SNV Data	0.98	0.97	0.97	4.81	5.28	4.79

In estimating the performance of TiN contained in TiN–MA and TiN–Al₂O₃, the coefficient of determination for the calibration (R²_{CAL}), cross-validation (R²_{CV}), and prediction (R²_{PRED}) values ranged between 0.48–0.86 wt% and those of RMSEC, RMSECV, and RMSEP were between 11–18.10 wt% for the raw Raman spectra data. Additionally, Raman spectra data pre-processed using SNV provided estimated values for R²_{CAL}, R²_{CV}, and R²_{PRED} varied between 0.84–0.99 and values for RMSEC, RMSECV, and RMSEP were between 2.60–9.07 wt% based on the model for evaluating the phase content of TiN binary samples TiN–(Al₂O₃, MA), as presented in Table 5. A similar trend could be observed for the assessment parameter in predicting the phase content for Ti₂O₃ in binary samples prepared from Ti₂O₃–(Al₂O₃, MA), as presented in Table 6. The PLS model for the raw Raman data had R²_{CAL}, R²_{CV}, and R²_{PRED} values ranging between 0.93–0.98, with RMSEC, RMSECV, and RMSEP values varying between 2.98–6.50 wt% for Ti₂O₃ analyses in these

samples. Estimating the individual phases by using SNV, the coefficient of determination (R^2_{CAL} , R^2_{CV} , and R^2_{PRED}) values varied between 0.97–0.99 and RMSEC, RMSECV, and RMSEP values were between 2.95–5.30 wt% for estimation of the Ti_2O_3 phases present in the samples for this study.

4. Discussion

4.1. Observation of Specific Raman Peaks Relative to the Change in Phase Content

As demonstrated in Figures 2 and 3, the Raman spectra can be used to qualitatively predict the phase content present in the binary samples based on the relative intensity of the Raman peaks associated with a specific phase. For TiN– Al_2O_3 and TiN–MA, medium Raman peaks at 157 cm^{-1} for TiN, at 383 cm^{-1} for Al_2O_3 , and approximately 773 cm^{-1} for MA were used to explain the phenomenon of a change in phase content having a corresponding effect on the relative Raman peaks. In Figure 3, observation based on variation in the phase fraction and the related impact on the relative Raman peak was examined for binary samples of Ti_2O_3 – $MgO\cdot Al_2O_3$, and Ti_2O_3 – Al_2O_3 . In these binary samples, and illustrated in Figure 3, Raman peaks at 247 and 335 cm^{-1} associated with Ti_2O_3 , at 416 and 773 cm^{-1} attributable to MA, and 383 , 422 , and 760 cm^{-1} associated with Al_2O_3 can be used in predicting the most dominating phase present in the sample mixtures. For sample mixtures of TiN– Al_2O_3 and TiN–MA, as presented in Figure 2, the phases (TiN, Al_2O_3 , and MA) had their most intense peaks quite close to each other, within the Raman band region between 410 – 460 cm^{-1} . Therefore, due to the effect of overlap of Raman peaks, the medium peaks were used for qualitative analysis. However, with the binary samples of Ti_2O_3 – $MgO\cdot Al_2O_3$ and Ti_2O_3 – Al_2O_3 , the most intense Raman peaks were used to observe the effect of a change in phase content and the relative Raman peak intensity since the potential peak overlap was not a challenge.

The estimation for MA phase content analysis in Ti_2O_3 – $MgO\cdot Al_2O_3$ and TiN– $MgO\cdot Al_2O_3$ based on the relative Raman peak area is shown in Table 4 (i and ii). The most suitable Raman peak area ratio with the best coefficient of determination value ($R^2 = 0.98$) for Ti_2O_3 – $MgO\cdot Al_2O_3$ was obtained from 416 cm^{-1} for MA and 247 cm^{-1} for Ti_2O_3 from a linear regression between the phase content and the relative Raman peak area. Similarly, to estimate the MA phase content for TiN– $MgO\cdot Al_2O_3$ samples, Table 4 (ii) shows that the relative Raman peak area ratios of $416/157$ and $773/157$ (157 cm^{-1} for TiN and 416 773 cm^{-1} for MA) had an excellent coefficient of determination value of 0.98 linear regression.

For binary sample systems of Ti_2O_3 – Al_2O_3 , the linear regression plotted between the phase content and the relative Raman peak area, the phase content for Al_2O_3 was estimated as shown in Table 4 (ii), with the identified Raman peak ratio at 422 cm^{-1} for Al_2O_3 and 247 cm^{-1} for Al_2O_3 having an R^2 value of 0.97 as the best. An estimation for Al_2O_3 content in Ti_2O_3 – Al_2O_3 also showed the best candidate peaks based on linear regression analysis to be 382 , 760 cm^{-1} for Al_2O_3 at approximately 157 cm^{-1} for TiN, with coefficient of determination values ranging between 0.98–0.99. Thus, Table 4 demonstrates Raman peak areas at approximately 157 cm^{-1} attributable to TiN, 382 , 422 , and 760 cm^{-1} associated with Al_2O_3 and at 416 and 773 cm^{-1} for MA as excellent indicators for the specific phases in the samples. Therefore, it can be concluded that integrated relative Raman peak areas as a function of the phase content present was a suitable method for the quantitative analysis in this study.

4.2. Further Phase Identification Evaluation

The analysis results obtained for each specific phase of TiN, Al_2O_3 , Ti_2O_3 , and $MgO\cdot Al_2O_3$ (MA), contained in the TiN– Al_2O_3 , TiN–MA, Ti_2O_3 –MA, and Ti_2O_3 – Al_2O_3 samples, showed excellent figures of merit, as illustrated in Tables 5 and 6. For the Raman data used in conducting the PLS regression model, all of the coefficients of determination (R^2_{CAL} , R^2_{CV} and R^2_{PRED}) values for estimating the specific phases ranged between 0.48–0.98. It should be noted that the low R^2 (R^2_{CAL} , R^2_{CV} and R^2_{PRED}) values, such as 0.48, were obtained from estimating individual phases of TiN and $MgO\cdot Al_2O_3$ from the

binary system of TiN–MgO·Al₂O₃, as shown in Table 5. In addition, for the SNV-treated Raman spectra data, the PLS regression model estimated (R^2_{CAL} , R^2_{CV} , and R^2_{PRED}) values to be between 0.94–0.99. It was observed from the R^2 values obtained for both the Raman data and the pre-processed data that Raman difference had a relatively broader range in predicting the individual phases present in the samples.

Additionally, as shown Tables 5 and 6, the PLS regression model was carried out on the raw Raman data and pre-processed (SNV) data. The figures of merit demonstrated that the estimated respective values for the root mean standard error features, such as RMSEC, RMSECV, and RMSEP, were generally improved when the raw Raman data were processed. For instance, from Table 5, the average values for predicting individual phases in TiN–(Al₂O₃ or MA) based on raw Raman data gave a coefficient of determination (R^2_{CAL} , R^2_{CV} and R^2_{PRED}) = 0.72 and root mean standard error features (RMSEC, RMSECV, and RMSEP) = 14.24 wt%. However, SNV Raman data displayed the average values of R^2_{CAL} , R^2_{CV} , and R^2_{PRED} = 0.96 and (RMSEC, RMSECV, and RMSEP) = 5.35 wt%. Based on the figures of merit from the PLS regression model, individual phases present in the binary synthetic inclusion system can be estimated from the prepared samples measured with Raman spectroscopy. Consequently, based on performance parameters (figure of merits), the analysis results obtained from pre-processed Raman spectra data (using SNV) improved compared with the raw Raman data results illustrated in Tables 5 and 6.

4.3. Potential Limitations in the Measurements and Prospect for Future Application

Some potential limitations attributable to the application of Raman spectroscopy for characterizing the synthetic samples in this study could include a slight instrumental variation, the penetration depth of laser, and the potentially heterogeneous nature of the sample mixtures prepared. In addition, some of the generally expected instrumental operational challenges could be associated with variations in incident laser power, such as potential sample heating or influence of fluorescence, which could adversely impact the quality of the measured Raman spectra. In addition, it can be safely assumed that inclusion found in an actual steel samples matrix could be more heterogeneous compared to the synthetic inclusion sample prepared for this study. The limitations associated with instrumental variation and the possible heterogeneous state of samples were mitigated in this study by using a sample holder with a rotating stage and measuring the same sample, on average, three times under a relatively wide laser spot size. Furthermore, the potential effect of fluorescence on the Raman spectra was suppressed based on the type of Raman spectroscopy (time-gated) used for the measurement, as demonstrated by Lipiäinen et al. [27]. It should be noted that Raman spectroscopy characterization is generally considered to be a surface analysis technique; therefore, the bulk composition of phases present in the samples could be obtained from extrapolation estimated from the planar distribution of phase analysis results.

This study demonstrated the prospect of using Raman spectroscopy for characterizing Ti-based (TiN and Ti₂O₃) inclusions combined with other detrimental oxide phases of Al₂O₃ and MgO·Al₂O₃ spinel inclusion types in steel samples, assuming the steel matrix to be Raman-inactive. The calibration models used in this work have been demonstrated to be a promising method for quantifying inclusion phases. Furthermore, combined with the previous studies [10,20], future inclusion characterization of steel samples could be enhanced by applying the Raman spectroscopy, thereby offering an opportunity for a potential reference database of inclusion characteristics of steel samples.

This study presents the prospect of contributing to the numerous studies [6–8,12,13,28–30] already conducted concerning the formation process and generation of data characterized in this work by using Raman spectroscopy to assist in identifying and predicting phase content, including that of Al₂O₃, Ti₂O₃, and MgO·Al₂O₃, in a multiphase system. For instance, this technique could be used to estimate the phase content of Ti₂O₃ and MgO·Al₂O₃ from a MgO–Al₂O₃–Ti₂O₃ system, as demonstrated by Ren et al. [28], who established equilibrium phases in their study. In addition, this could be used in the future to predict the phase

content of $\text{MgO}\cdot\text{Al}_2\text{O}_3$, Ti_2O_3 , or Al_2O_3 from the formation of $\text{MgO}\cdot\text{Al}_2\text{O}_3\text{--Ti}_2\text{O}_3$ -based inclusions obtained from the reaction associated with soluble Ti and $\text{MgO}\cdot\text{Al}_2\text{O}_3$ [29] and for the characterization of complex Al-Ti oxide formations, with Al_2O_3 in the core and Ti_2O_3 on the surface [30].

The utilization of Raman spectroscopy as an analytical method presents some advantages over known conventional techniques such as scanning electron microscopy equipped with energy-dispersive spectroscopy [6,8,29], cathodoluminescence (CL) [31], and others outlined by Zhang et al. (2003) [9] used for the identification and classification of inclusion in steel. Some of the merits of using Raman spectroscopy include the relatively shorter duration needed for sample preparation, acquisition and analysis of the results, and a prospect for both the qualitative and quantitative characterization for Raman-active materials [32]. Additionally, most non-metallic inclusions, such as calcium aluminates and Ti-based phases, are Raman active, and steel is considered Raman inactive. Consequently, the Raman spectra measured from steel samples are regarded as originating from the inclusions found within the steel matrix and identified based on the fingerprint of the specific component present in the steel sample.

5. Conclusions

Raman spectroscopy, combined with calibration models such as PLS regression in this study, has demonstrated its suitability for qualitative and quantitative analysis to estimate the relative phase content for different sets of binary samples consisting of synthetic phases Al_2O_3 , TiN, Ti_2O_3 , and $\text{MgO}\cdot\text{Al}_2\text{O}_3$. The main findings obtained from this work are summarized as follows:

1. The most suitable Raman peaks (bands) identified for estimating the phases content present in the samples were:
 - For $\text{Ti}_2\text{O}_3\text{--MA}$ and $\text{Ti}_2\text{O}_3\text{--Al}_2\text{O}_3$ samples: at 247 cm^{-1} for Ti_2O_3 , at 416 and 773 cm^{-1} for $\text{MgO}\cdot\text{Al}_2\text{O}_3$, and 383, 422, and 760 cm^{-1} for Al_2O_3 .
 - For $\text{TiN--Al}_2\text{O}_3$ and TiN--MA samples: Raman peaks at 157 cm^{-1} for TiN, at 773 cm^{-1} for $\text{MgO}\cdot\text{Al}_2\text{O}_3$, and 383 cm^{-1} for Al_2O_3 .
2. The Raman spectra data pre-processed by using the SNV had improved statistical performance, such as R^2 , RMSECV, and RMSEP, in the evaluation of the phase contents compared to the analysis made using the raw Raman spectra data.
3. This work and previous studies combined present the prospect of using Raman spectroscopy to characterize a complex multiphase system that may contain oxide- and nitride-based inclusions in steel samples.

Author Contributions: F.G. conducted the experiments and wrote the paper, and all the authors (F.G., T.A., Q.S., M.A., and T.F.) contributed to its results and discussion. All authors have read and agreed to the published version of the manuscript.

Funding: This research received no external funding.

Institutional Review Board Statement: Not applicable.

Informed Consent Statement: Not applicable.

Data Availability Statement: Not applicable.

Acknowledgments: Corresponding author (F.G.) wish to acknowledge the personal research grant (grant number: 1449) support received from the Technology Industries of Finland Centennial Foundation under Steel and Metal Producers' Fund, Finland under the project topic; the application of Raman spectroscopy for the study of nonmetallic inclusions found in steel matrix as an important criterion for assessing steel cleanliness.

Conflicts of Interest: The authors declare no conflict of interest.

References

1. Khare, S. Approximations in using solubility products for B, N, Ti and Al. *Mater. Sci. Technol.* **2011**, *27*, 1863–1868. [[CrossRef](#)]
2. Nagao, N. Strengthening and Toughening of Hot-direct-rolled Steels by Addition of a Small Amount of Titanium. *ISIJ Int.* **1989**, *29*, 940–946.
3. Baker, T.N. Titanium Microalloyed Steels. *Ironmak. Steelmak.* **2019**, *46*, 1–55. [[CrossRef](#)]
4. Burja, J.; Koležnik, M.; Župerl, S.; Klančnik, G. Nitrogen and Nitride Non-metallic Inclusions in Steel. *Mater. Tehmol.* **2019**, *53*, 919–928. [[CrossRef](#)]
5. Zhu, Y.; Lu, Y.-M.; Huang, C.-W.; Liang, Y.-L. The Effect of TiN Inclusions on the Fracture Mechanism of 20CrMnTi Steel with lath Martensite. *Mater. Res. Express* **2020**, *7*, 36509. [[CrossRef](#)]
6. Yan, W.; Shan, Y.Y.; Yang, K. Influence of TiN Inclusions on the Cleavage Fracture Behavior of Low-Carbon Microalloyed Steels. *Metall. Mater. Trans. A* **2007**, *38*, 1211–1222. [[CrossRef](#)]
7. Yang, L.; Cheng, G.-G.; Li, S.-J.; Zhao, M.; Feng, G.-P. Characteristics of MgAl₂O₄-TiN Complex Inclusion Precipitation and Growth during Solidification of GCr15SiMn in ESR Process. *ISIJ Int.* **2015**, *55*, 1693–1698. [[CrossRef](#)]
8. Wang, R.; Bao, Y.-P.; Yan, Z.-J.; Li, D.-Z.; Kang, Y. Comparison Between the Surface Defects Caused by Al₂O₃ and TiN Inclusions in Interstitial-free Steel Auto Sheets. *Int. J. Miner. Metall. Mater.* **2019**, *26*, 178–185. [[CrossRef](#)]
9. Zhang, L.; Thomas, B.G. State of the Art in Evaluation and Control of Steel Cleanliness. *ISIJ Int.* **2003**, *43*, 271–291. [[CrossRef](#)]
10. Gyakwaa, F.; Aula, M.; Alatarvas, T.; Vuolio, T.; Shu, Q.; Huttula, M.; Fabritius, T. Characterisation of Binary Phase Mixtures of Magnesium-Aluminate Spinel and Calcium-Aluminates Using Time-Gated Raman Spectroscopy. *ISIJ Int.* **2020**, *60*, 988–997. [[CrossRef](#)]
11. Li, S.; Hihara, L.H. Identification of Inclusions in Carbon Steels using Micro-Raman Spectroscopy. *J. Raman Spectrosc.* **2017**, *48*, 137–142. [[CrossRef](#)]
12. Matsuura, H.; Wang, C.; Wen, G.; Sridhar, S. The Transient Stages of Inclusion Evolution During Al and/or Ti Additions to Molten Iron. *ISIJ Int.* **2007**, *47*, 1265. [[CrossRef](#)]
13. Pan, C.; Hu, X.J.; Zheng, J.C.; Lin, P.; Chou, K.C. Effect of Calcium Content on Inclusions during the Ladle Furnace Refining Process of AISI 321 Stainless Steel. *Int. J. Miner. Metall. Mater.* **2020**, *27*, 1499–1507. [[CrossRef](#)]
14. Michelic, S.K.; Bernhard, C. Experimental Study on the Behavior of TiN and Ti₂O₃ Inclusions in Contact with CaO-Al₂O₃-SiO₂-MgO Slags. *Scanning* **2017**, *2017*, 2326750. [[CrossRef](#)]
15. Qi, J.-H.; Xue, Z.-L.; Wu, J.; Cheng, C.-G.; Gao, Y.-M. Ti-Deoxidized Products and Formation Mechanism of Intragranular Ferrite in High Grade Pipeline Steels. *J. Iron Steel Res. Int.* **2010**, *17*, 63–67. [[CrossRef](#)]
16. Barshilia, H.C.; Rajam, K.S. Raman spectroscopy studies on the thermal stability of TiN, CrN, TiAlN coatings and nanolayered TiN/CrN, TiAlN/CrN multilayer coatings. *J. Mater. Res.* **2004**, *19*, 3196–3205. [[CrossRef](#)]
17. Bradley, M. Lineshapes in IR and Raman Spectroscopy: A Primer. *Spectroscopy* **2015**, *30*, 42–46.
18. Asadena, P.; Alifornia, C. Quantitative Analysis Using Raman Spectrometry. *Appl. Spectrosc.* **2003**, *57*, 20A–42A.
19. Barnes, R.J.; Dhanoa, M.S.; Lister, S.J. Standard Normal Variate Transformation and De-trending of Near-infrared Diffuse Reflectance Spectra. *Appl. Spectrosc.* **1989**, *43*, 772–777. [[CrossRef](#)]
20. Gyakwaa, F.; Aula, M.; Alatarvas, T.; Shu, Q.; Huttula, M.; Fabritius, T. Quantification of Synthetic Nonmetallic Inclusion Multiphase Mixtures from a CaO-Al₂O₃-MgO-CaS System Using Raman Spectroscopy. *Steel Res. Int.* **2021**, *92*, 2000322. [[CrossRef](#)]
21. De Almeida, M.R.; Correa, D.N.; Rocha, W.F.C.; Scafi, F.J.O.; Poppi, R.J. Discrimination Between Authentic and Counterfeit Banknotes using Raman Spectroscopy and PLS-DA with Uncertainty Estimation. *Microchem. J.* **2013**, *109*, 170–177. [[CrossRef](#)]
22. Kachrimanis, K.; Braun, D.E.; Griesser, U.J. Quantitative Analysis of Paracetamol Polymorphs in Powder Mixtures by FT-Raman Spectroscopy and PLS Regression. *J. Pharm. Biomed. Anal.* **2007**, *43*, 407–412. [[CrossRef](#)] [[PubMed](#)]
23. Cheng, P.; Ye, T.; Zeng, H.; Ding, J. Raman Spectra Investigation on the Pressure-induced Phase Transition in Titanium Nitride (TiN). *AIP Adv.* **2020**, *10*, 45110. [[CrossRef](#)]
24. Misra, A.; Bist, H.D.; Navati, M.S.; Thareja, R.K.; Narayan, J. Thin Film of Aluminum Oxide Through Pulsed Laser Deposition: A Micro-Raman Study. *Mater. Sci. Eng.* **2001**, *79*, 49–54. [[CrossRef](#)]
25. Dash, S.; Sahoo, R.K.; Das, A.; Bajpai, S.; Debasish, D.; Singh, S.K. Synthesis of MgAl₂O₄ Spinel by Thermal Plasma and its Synergetic Structural Study. *J. Alloys Compd.* **2017**, *726*, 1186–1194. [[CrossRef](#)]
26. Chen, Y.; Mao, J. Sol-gel Preparation and Characterization of Black Titanium Oxides Ti₂O₃ and Ti₃O₅. *J. Mater. Sci. Mater. Electron.* **2014**, *25*, 1284–1288. [[CrossRef](#)]
27. Lipiäinen, T.; Pessi, J.; Movahedi, P.; Koivistoinen, J.; Kurki, L.; Tenhunen, M.; Yliruusi, J.; Juppö, A.M.; Heikkonen, J.; Pahikkala, T.; et al. Time-Gated Raman Spectroscopy for Quantitative Determination of Solid-State Forms of Fluorescent Pharmaceuticals. *Anal. Chem.* **2018**, *90*, 4832–4839. [[CrossRef](#)] [[PubMed](#)]
28. Ren, Y.; Zhang, L.; Yang, W.; Duan, H. Formation and Thermodynamics of Mg-Al-Ti-O Complex Inclusions in Mg-Al-Ti-Deoxidized Steel. *Metall. Mater. Trans. B* **2014**, *45*, 2057–2071. [[CrossRef](#)]
29. Zheng, D.; Li, J.; Shi, C.; Zhang, J.; Geng, R. Evolution of TiN and Oxide Inclusions in Ti-containing Fe-25Ni-15Cr Alloy during Electroslag Remelting. *ISIJ Int.* **2020**, *60*, 1577–1585. [[CrossRef](#)]
30. Byun, J.-S.; Shim, J.-H.; Cho, Y.W.; Lee, D.N. Non-metallic inclusion and intragranular nucleation of ferrite in Ti-killed C-Mn steel. *Acta Mater.* **2003**, *51*, 1593–1606. [[CrossRef](#)]

-
31. Imashuku, S.; Wagatsuma, K. Rapid Identification of Calcium Aluminate Inclusions in Steels Using Cathodoluminescence Analysis. *Metall. Mater. Trans. B* **2018**, *49*, 2868–2874. [[CrossRef](#)]
 32. Kontoyannis, C.G.; Bouropoulos, N.C.; Koutsoukos, P.G. Raman spectroscopy: A tool for the quantitative analysis of mineral components of solid mixtures. The case of calcium oxalate monohydrate and hydroxyapatite. *Vib. Spectrosc.* **1997**, *15*, 53–60. [[CrossRef](#)]